Kinetic Monte Carlo Study of Submonolayer Heteroepitaxial Growth Comparing Cu/Ni and Pt/Ni on Ni(100)

Kenneth Haug,* Myat Lin, and Nathaniel J. Lonergan

Department of Chemistry, Lafayette College, Easton, Pennsylvania 18042

Received: March 22, 2005

The surface patterns formed during submonolayer Cu/Ni and Pt/Ni heteroepitaxy upon a Ni(100) substrate have been investigated by kinetic Monte Carlo (KMC) simulations. The two-dimensional (2D) KMC simulations are based upon rate constants for a complete nearest-neighbor set of 729 uncorrelated Cu or Pt atoms and/or Ni site-to-site hopping mobilities. The rate constant activation energies are determined by classical-potential total-energy calculations using an embedded-atom method potential function from the literature. We find that diffusion of Cu atoms occurs at a faster rate and Pt atoms at a slower rate than that of Ni atoms on the flat Ni(100) surface, and the initial nucleation and growth patterns of 2D islands and the kinetic versus thermodynamic control of the growth vary as a consequence. In the temperature and deposition time regime in which we work, the Cu/Ni systems show less than random mixing, while the Pt/Ni systems show more than random mixing. The Cu/Ni system has bonding energies that result in a tendency to segregate toward subdomains of pure Ni and Cu, though kinetic effects in the epitaxy trap the development of the system at small subdomain sizes. The Pt/Ni system has bonding energies giving a tendency to intermix completely, while epitaxial kinetic effects modestly interfere with the complete mixing. The kinetically determined island morphologies under various Cu/Ni and Pt/Ni compositions and deposition rates differ substantially over time periods that are long on the deposition time scale, and therefore the island patterns can become frozen in place.

I. Introduction

An experimental understanding of the epitaxial growth of metallic and bimetallic thin films has received a great deal of investigation in recent years. In addition to its intrinsic interest, much of this work is also stimulated by applications involving microelectronic devices and the nano-design of more effective catalysts. In this paper, we are examining the epitaxial growth of two complementary bimetallic systems: Cu/Ni and Pt/Ni. The Cu/Ni thin film interface has seen a great deal of theoretical and experimental investigation due to its importance as circuit interconnects for magnetic devices[1–6] and for sensor systems.[7] The Pt/Ni thin film interface is also of interest, principally due to the nanocatalytic properties of Pt on various supports, including as an alloy in Ni,[8–13] such as the specific variations in catalytic pathways for some organic reactions due to thin Pt overlayers on Ni.[14,15] We also view the Cu/Ni and Pt/Ni systems as complementary because, within our theoretical treatment, the interaction energies complement each other in ways that allow the two systems to serve as a model of the differing relative roles for the kinetic and thermodynamic effects in epitaxial growth, itself a topic of interest.[4,16,17]

A first step in understanding the properties of epitaxially grown metal surfaces is a better understanding of the growth itself, in particular an understanding of the pattern formation of the developing surface islands and for bimetallic systems an understanding of each metal's distribution within those islands, since these features will help determine the electronic, magnetic, and catalytic properties of the thin film.[9] The growth patterns can generally be described in terms of the competition of the rates for various processes involved: the deposition rate, the mobility rate of a lone adatom across a surface, the condensation of a lone adatom with other adatoms to form islands, the evaporation of such islands, and the peripheral diffusion of atoms along the edge of an island. Are the rates such that kinetic factors govern the growth, or do the thermodynamic forces of the interaction energies govern the growth? We examine these issues for the Cu/Ni and Pt/Ni growth interfaces by carrying out submonolayer kinetic Monte Carlo (KMC) simulations that examine the heteroepitaxial growth patterns as Cu or Pt and Ni are deposited on the Ni(100) surface. The KMC computations, in turn, are governed by a set of reasonable activation energies for the component processes, derived from a realistic, though imperfect, potential energy surface (PES). We use an embedded-atom PES formalism in the form given by Foiles, Baskes, and Daw[18] (and noted in more detail below), and within that PES formalism, the interaction energies and mobilities of the Cu/Ni and Pt/Ni systems vary by roughly equal amounts, but in opposite directions, as compared to the Ni/Ni system for a Ni(100) starting substrate. The Cu/Ni interaction is weaker, the Cu mobility faster, the Pt/Ni interaction stronger, and the Pt mobility slower, than the pure Ni/Ni system itself. The result of these effects is that, at the model level, the Cu/Ni and Pt/Ni systems display island pattern variations and differences in the kinetic versus thermodynamic control of those patterns as the KMC plays itself out. Experimental and theoretical surface segregation studies for Cu/Ni[19–23] and Pt/Ni[24–26] surfaces have been reported. The theoretical studies[19,24,26] have used either the same or somewhat modified embedded-atom method (EAM) potentials to that which we are using, although usually at temperatures in the 800–1500 K range for comparison with

* Author to whom correspondence should be addressed. E-mail: haugk@lafayette.edu.

the experiments in that same range. The theoretical studies[19,24,26] have also used exchange Monte Carlo rather than KMC since their interests were in exploring the thermodynamic properties of the alloy surfaces. Our own interest is in the kinetic evolution of surface patterns during epitaxial growth at much lower temperatures (around 250 K) where kinetic factors may be expected to have a large role in the surface structure. So while not directly comparable to the epitaxial surface pattern study and temperature of our own work, it is worth commenting briefly on these previous experimental−theoretical comparisons since they support the adequacy of the EAM model and give some support to the conclusions of our own KMC study.

In the Cu/Ni case,[19−23] surface segregation of Cu was reported in a comparison of theory[19] with experiment[20−23] for a variety of bulk Cu/Ni alloys at a temperature of 800 K. The top layer of both (111) and (100) faces of Cu/Ni alloys with bulk atomic percent Cu ranging from around 5% to 50% were reported (in both experiment and in theoretical calculations) to have Cu present in the 80−98 atomic percent range. In the subsurface layers (reported in the theoretical calculations), Cu was found in substantially diminished composition in the second and third layers and roughly recovers the bulk composition pattern by the fourth to fifth layer. These results connect to our own epitaxial studies, reported below, where we also find a preference by Cu in $Cu_{50}Ni_{50}$ alloys growing on pure bulk Ni(100) for the outer edge of islands that form in the growth layer, which we analyze in terms of the interaction energies and activation barriers involved in our KMC simulations.

In the Pt/Ni case,[24−30] in the 800−1500 K temperature range, surfaces enriched in Pt have been reported for the bulk Pt_{50}/Ni_{50} alloy for the (100) and (111) surfaces, with Ni dominating the (110) surface. These studies have shown a qualitative agreement in surface segregation pattern discrepancy between theory[24,25] and experiment[26−30] (recently summarized in ref 25) but with more deviations as compared to Cu/Ni noted above. The segregation patterns in the bulk alloys depend very critically on the particular face exposed. For example, the top layer of the (111) face of the Pt_{50}/Ni_{50} alloy was reported in both theory[24,25] and experiment[26−30] to have Pt present in the 70−95 atomic percent range. In the second layer, Pt was found in diminished composition and roughly recovered the bulk composition pattern by an alternating increase and decrease in composition by the fourth to fifth layer. The top layer of the (110) face of the Pt_{50}/Ni_{50} alloy was reported to have Pt present in the 0−40 atomic percent range, while in the second layer, Pt was found in substantial composition (80−100%) and again roughly recovered the bulk composition pattern by an alternating increase and decrease in composition by the fourth to fifth layer. On the (100) surface, the experiments[26,27] reported Pt enhancement, but theoretical calculations were not compared for this surface. Very recently, Monte Carlo simulations using modified EAM potentials for Pt−Ni nanoparticles containing between 586 and 4033 atoms have also shown equilibrium structures at $T = 600$ K with Pt enrichment in the outermost and third layer and with Ni enriched in the second layer.[31] In our epitaxial studies, reported below for Pt_{50}/Ni_{50} epitaxially growing on pure bulk Ni(100), we find a preference for the Pt and Ni to intermix considerably in the growth layer though with Pt showing a slight preference for the outer edge of growing islands, which we again analyze in terms of the interaction energies and activation barriers involved in our KMC simulations.

II. Theoretical and Computational Results

Since the hopping of an adsorbed adatom (Cu, Pt, or Ni in our case) from one binding site to another nearest-neighbor site

on the Ni(100) surface is a rare event at the temperatures that interest us (for example, at 250 K the hopping time for the Ni adatom is on the order of 10^{-3} s, while the vibrational period in the binding site is on the order of 10^{-13}s), a direct simulation of the growth process is computationally cumbersome. In our work, we account for the time separation by dividing the theoretical description of the growth into a two-part process, first calculating thermal activation energies for a set of individual hopping events, which give thermal rate constants for the hopping events via transition state theory (TST), and second using a KMC simulation of the deposition and growth process based upon the set of thermal rate constants. In the following, we examine each of these components in turn.

A. Activation Barrier Energies. The method that we use to calculate the activation energies is given in more detail in some of our previous work.[32] Here we briefly review the method. The activation energies are calculated using a slab of Ni consisting of 113 dynamically active Ni atoms arranged in three face-centered cubic (fcc) layers with the (100) face exposed. The active atoms were surrounded by a rigid basin consisting of two fcc layers of Ni atoms in equilibrium positions that make up the "bottom" and "sides" of the basin. The combined number of active and rigid Ni atoms making up this slab is 450. The island adatoms (Ni and Cu or Pt) are placed in the central area of the surface slab. To simulate island condensation and evaporation events, we use up to 16 adatoms in a variety of configurations (noted below). All of the active slab atoms along with the surface adatoms are free to move. To determine the energy barrier height for the various hopping events, we first determine initial relaxed configurations for all of the dynamically active molecules by starting from the rigid lattice atom positions, by use of damped molecular dynamics until equilibrium positions are found. The minimum-energy profile along the reaction path connecting the initial and final configuration is then mapped out by a restricted total-energy relaxation scheme in which one degree of freedom (one coordinate of one atom) is fixed at a set of intervals connecting the initial and final configurations, while all other degrees of freedom are fully relaxed. The specific interaction energy used for modeling the system is the EAM potential energy given by Foiles, Baskes, and Daw for a variety of fcc metals,[18] as implemented by Plimpton and Hendrickson in the ParaDyn code[33] This approach offers a realistic, though imperfect, representation of the metals examined here and has been used in a wide variety of applications.[34] In particular, in previous applications to Cu/Ni[19] and Pt/Ni[24] surfaces, reasonably good agreement of EAM results with experimental results have been noted. An important factor for us in choosing this potential set (over other potentials for Ni, Cu, and Pt that individually may be more accurate) is that the atoms are represented using a consistent theoretical treatment, and this avoids any extra theoretical biases when any of the two metals are combined or when pairs of the metals are compared.

The adatoms on Ni(100) all attach preferentially to the fcc 4-fold hollow site with binding energies of 2.99, 3.67, and 5.16 eV for Cu, Ni, and Pt, respectively. With the procedure noted above, we have calculated a set of rate constants for lone atom mobility, condensation, evaporation, and peripheral-edge diffusion events. A few of these hopping processes are summarized in Table 1, along with the energy barriers and time constants, defined by eq 2 below, for the hopping process. Our KMC simulations, reported below, make use of the complete set of uncorrelated single hopping events as denoted in Figure 1a, which gives rise to a total of $3^6 = 729$ rate constants for

TABLE 1: Sampling of Activation Barrier Energies, E, and Time Constants, τ, from Equation 2 Evaluated at 250 K, for Selected Hopping Events Discussed in the Text[a]

| | mobile atom | | | | | |
| | Ni | | Cu | | Pt | |
event on Ni(100) terrace	E (eV)	τ (s)	E (eV)	τ (s)	E (eV)	τ (s)
lone atom hopping	0.62	0.61(+0)	0.52	5.8(−3)	0.74	1.6(+2)
Peripheral Diffusion						
along Ni edge	0.33	8.7(−7)	0.28	8.5(−8)	0.37	5.5(−6)
along Cu edge	0.37	5.5(−6)	0.31	3.4(−7)		
along Pt edge	0.31	3.4(−7)			0.47	5.8(−4)
Condensation						
corner attachment to Ni	0.27	5.3(−8)	0.22	5.2(−9)	0.26	3.4(−7)
sliding attachment to Ni	0.30	2.2(−7)	0.25	2.1(−8)	0.31	3.4(−7)
edge attachment to Ni	0.58	9.5(−2)	0.48	9.2(−4)	0.67	6.2(+0)
corner attachment to Cu	0.31	3.4(−7)	0.25	2.1(−8)		
sliding attachment to Cu	0.34	1.4(−6)	0.28	8.5(−8)		
edge attachment to Cu	0.57	6.0(−2)	0.47	5.8(−4)		
corner attachment to Pt	0.21	3.3(−9)			0.36	3.5(−6)
sliding attachment to Pt	0.25	2.1(−8)			0.43	9.0(−5)
edge attachment to Pt	0.56	3.8(−2)			0.64	1.5(+0)
Evaporation						
sliding detachment from Ni	0.67	6.2(+0)	0.58	9.5(−2)	0.80	2.6(+3)
corner detachment from Ni	1.02	7.1(+7)	0.89	1.7(+5)	1.24	1.9(+12)
edge detachment from Ni	1.03	1.1(+8)	0.92	6.8(+5)	1.32	7.9(+13)
sliding detachment from Cu	0.66	3.9(+0)	0.57	6.0(−2)		
corner detachment from Cu	0.95	2.8(+6)	0.83	1.0(+4)		
edge detachment from Cu	0.98	1.1(+7)	0.86	4.2(+4)		
sliding detachment from Pt	0.65	2.5(+0)			0.76	4.1(+2)
corner detachment from Pt	1.01	4.5(+7)			1.03	1.1(+8)
edge detachment from Pt	1.06	4.5(+8)			1.15	3.0(+10)

[a] The values for τ are denoted such that 5.1(−10) is equal to 5.1×10^{-10}. A blank indicates that the corresponding hopping process is not considered in this study.
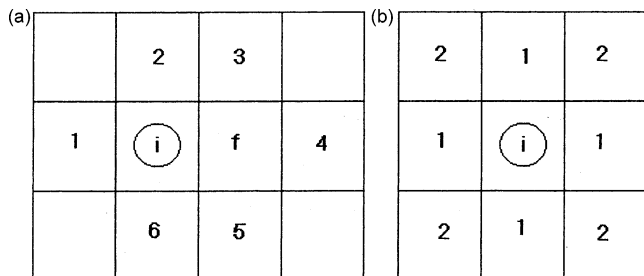

Figure 1. 1. (a) Adatom site labels for the (100) hoping processes with notation as discussed in the text. (b) Notation used for the first two shells of the Cowley short-range order parameter defined in eq 5 of the text.

eachadatom type (giving a total of 1458 for the Cu/Ni system and 1458 for the Pt/Ni system). A number of these rate constants are equivalent by symmetry, of course, and symmetry also gives us the forward and reverse rate constants for hopping events so that detailed balance is readily built into our KMC simulation. We have calculated, but do not include in the KMC simulation, any surface layer to adlayer exchanges. On the Ni(100) surface, for the PES that we are using, these events have high energy barriers, for example about 1.35 eV for a lone Ni adatom, with correspondingly very low probabilities of exchange occurring in the KMC simulation at the temperatures that interest us (around 250 K). Since only the set of rates noted in Figure 1a are used in the KMC simulations, it is also important to note that long-range strain effects are not being incorporated, which restricts the scope of KMC reliability—long-range ordering will not be seen.

The Ni, Cu, and Pt adatoms on Ni(100) move from site to site with an increasing trend in activation energy in the Cu, Ni,

Pt order (see line 1 of Table 1), which also is the order of the bonding energies noted above. For example, a lone adatom hopping from site to site on the flat Ni(100) terrace has an activation energy barrier that is 0.52, 0.61, and 0.74 eV for Cu, Ni, and Pt, respectively. For the Ni/Ni(100) self-diffusion, the EAM activation energy can be compared favorably with a value of 0.63 eV estimated from field ion microscopy,[35] and although we are not acquainted with experimental estimates for the activation energies of the Cu and Pt species on Ni, the equilibrium values appear to be in reasonable agreement with experiment as noted above in regards to the higher temperature studies of refs 19−30. The effect of the Cu, Ni, and Pt differences in energy barriers is an acceleration of island formation for the Cu adatoms islands and a deceleration of the formation of Pt adatom islands as compared to the Ni island formation. In addition to having lower lone atom hopping activation energy, the three adatom types also have modified activation energies for island evaporation and condensation processes. Selected condensation and evaporation barriers are also noted in Table 1, described here by the use of notation from Figure 1a; "corner attachment" indicates a move from i → f with sites 4 and 5 occupied, "edge attachment" indicates that move with site 4 occupied, "sliding attachment" indicates that move with site 5 occupied, and the "detachment" processes in Table 1 are the reverse of those just noted. As a specific case of the condensation process noted in the activation barriers in line 7 of Table 1, the condensation of a Ni adatom attaching to a Ni island by a straight edge attachment has a barrier of 0.58 eV, while Cu and Pt adatoms have barriers of 0.48 and 0.67 eV, respectively. The evaporation processes show similar variations; for example, in line 16 of Table 1, the evaporation process of a Ni adatom detaching from a Ni island along a straight edge has a barrier of 1.03 eV, while Cu and Pt adatoms

TABLE 2: Adatom Dimer Bonding Energies for Selected Dimers Adsorbed on the Ni(100) Terrace

direct pure dimers	bond E (eV)	direct mixed dimers	bond E (eV)
Ni−Ni	−0.42	Ni−Cu	−0.37
Cu−Cu	−0.33	Ni−Pt	−0.53
Pt−Pt	−0.46		

diagonal pure dimers	bond E (eV)	diagonal mixed dimers	bond E (eV)
Ni−Ni	−0.06	Ni−Cu	−0.07
Cu−Cu	−0.08	Ni−Pt	−0.13
Pt−Pt	−0.20		

have barriers of 0.92 and 1.32 eV, respectively. A variety of other condensation and evaporation events are also given in Table 1, and they show generally similar effects. Of course, it is the joint condensation/evaporation processes that by detailed balance give the island binding energies, given in Table 2 for the diatomic adatom islands, and these binding energies control the thermodynamic patterns of the surface. (Note that in Table 2 we report the diatomic binding energies, while the condensation/evaporation barriers in Table 1 are reported for 16 atom islands, which accounts for the minor discrepancies.) One of our interests here is to explore, via the KMC simulations, how the kinetic patterns governed by the barrier heights differ from and/or approach equilibrium thermodynamic patterns. From the diatomic binding energies in Table 2, the Cu/Ni surface is expected to mix nearly randomly since the Cu−Ni bonding energy lies roughly midway between the Cu−Cu and Ni−Ni bonding energies. Therefore, in a 50−50 mixture of Cu and Ni adatoms, the energy loss in going from Ni−Ni to Cu−Ni bonds is made up by the energy gain in going from Cu−Cu to Cu−Ni bonds. The thermodynamic Pt/Ni surface is significantly different based upon the diatomic binding energies, which drive the Pt/Ni toward a complete (rather than random) mixing, tending toward an alternating checkerboard pattern that maximizes the number of deep energy Pt−Ni bonds.

B. KMC Method. The KMC method is a stochastic solution of the master equation governing the deposition and growth processes occurring in this system.[36] It is based upon the assumption that the hopping events are random. (The separation between vibrational and translational time periods noted above suggests that the hopping events are reasonably random in the present case.) With the calculated activation energies, E_{act}, for a given hopping event taken from the calculations discussed in section IIA above, the rate constant for the event is assumed to follow from TST as

$$k = (k_B T/h)(Q^{\#}/Q) \exp(-E_{act}/k_B T) \approx (k_B T/h) \exp(-E_{act}/k_B T) \quad (1)$$

where k_B is Boltzmann's constant, T is the temperature, h is Planck's constant, and $Q(Q^{\#})$ is the vibrational partition function of the reactant (transition state) configuration. In test calculations, the vibrational partition function ratio ($Q^{\#}/Q$) for the Ni hopping events is on the order of unity, and we set it equal to unity in all of the KMC simulations discussed here. This is also reasonable since quantitative errors in E_{act} due to flaws in the potential energy function will probably swamp the $Q^{\#}/Q$ term variations in any case.

To more easily compare the relative hopping rates used in our KMC study, we have also included in Table 1 the time constants τ for each hopping process noted there, defined as

$$\tau = 1/k \quad (2)$$

where k is the rate constant from eq 1 above evaluated at $T = 250$ K, a low-end temperature taken from some epitaxial growth experiments,[3,37] although we also explore a small range of temperatures in the KMC simulations below. For comparison purposes, an experimental deposition time scale, which we use in the results presented below, is one monolayer deposition time on the order of 500 s, and we also explore deposition times (t_{dep}) from 50 to 500 s below.[3,37]

We follow a KMC procedure similar to that outlined by Lu and Metiu,[38] with our particular algorithm more completely described in Haug et al.[32] The general KMC procedure is used by many groups modeling surface growth, and variations in the algorithms exist. Here we very briefly note a few points to specify the algorithm that we use. The adatoms are deposited on the surface with a specified deposition rate and then are moved from site to site with probabilities for a move proportional to the appropriate rate constant using Arrhenius (or transition state) kinetics for the move via[36,38]

$$P_i = k_i/k_{ref} \quad (3)$$

where k_i is the rate constant, from eq 1 for event "i", which refers to a given adatom hopping event from the 1458 possible configuration events noted in section IIA, and k_{ref} is taken to be the rate constant corresponding to the fastest relevant process among those that we wish to distinguish.[39] We use a specified constant deposition rate[38] rather than a stochastic deposition rate[40,41] since our focus is to compare the surface dynamic differences between the Cu/Ni and Pt/Ni systems and control of the deposition clarifies that comparison. This simplification is unrealistic in that it assumes equal deposition rates and sticking coefficients for each metal onto the Ni substrate, and the two-dimensional (2D) nature of the simulation further assumes that further Cu and Pt atoms do not deposit on previous Cu or Pt.

In KMC applications with widespread time scales, a variety of approaches have been used for the time increment including recent multiscale algorithms[40,41] in addition to more conventional fixed[38] and stochastic[36] time increments. While a general review of these algorithms is beyond the scope of this paper, we do wish to note that our approach to Monte Carlo time uses the fixed increment approach,[38,39,42] giving an average proportionality to real time, rather than the stochastic process,[36,40,41,43] which can ensure an exact correspondence of Monte Carlo time with real time. This choice is due in part to the approximations in the potential and the approximation of 2D growth, so that suggesting an exact time seems inappropriate to our overriding interest in simplifying the cross-system comparisons through fixed control of the clock unit step. The value of k_{ref} sets the digital clock unit step for the system, so all processes happening faster than the reference rate are not distinguished. For the studies reported here, k_{ref} is determined by a reference activation energy, typically 0.37 eV ($\tau = 5.5 \times 10^{-6}$ s at 250 K) for the Cu−Ni system and 0.42 eV ($\tau = 5.6 \times 10^{-5}$ s at 250 K) for the "slower" Pt−Ni system. These choices do effectively distinguish the lone atom hopping rates from the evaporation rates and from most of the condensation rates. These three categories are of greatest importance in determining adatom island size, but the choice of reference energy does not distinguish many of the peripheral diffusion rates. As noted by Uebing,[39] one needs to be careful in such cases, and we have therefore tested several models in which significantly smaller and larger reference rates were used (with details reported in the Appendix), and we found no statistically significant differences in the observables for the set of rate processes used in

Heteroepitaxial Growth of Cu and Pt on Ni(100)

J. Phys. Chem. B, Vol. 109, No. 30, 2005 **14561**

our KMC. Therefore, we believe that we are distinguishing the rates of the most relevant events in the growth processes that govern the growth patterns of these surfaces.

As noted above, the KMC builds in only local strain effects in nearest-neighbor bonding patterns but does not build in long-range strain and resulting reorganizations. For example, experimentally[3] the growth of pure Cu on Ni(100) has been found to form Cu "stripes" beginning at about 0.25 to full monolayer (ML) coverage at temperatures and deposition rates similar to those examined here, which is believed to be due to the relaxation of accumulating compressive strain. Therefore, all of the results reported here involve simulating the deposition of submonolayer (with typical combined coverages on the order of 0.5 ML, but up to a full monolayer coverage for less-than-realistic but interesting test cases) of Cu/Ni or Pt/Ni adatoms onto a Ni(100) surface. The typical cases in our study involve equal mixing of two miscible metals in the epitaxial growth layer, lessening the extent of strain accumulation over long ranges that may break the (100) symmetry. The KMC model uses periodic boundary conditions so that if any adatom leaves the surface on one side of the 2D arena it will instantaneously reappear on the other side. The simulations use a 2D lattice representing the (100) cut of the Ni fcc crystal with a surface size of 40 × 40 sites. Several other grid sizes were tested to ensure that those periodic boundary conditions did not display significant correlation effects from side to side of the grid. Several computational experiments are performed to determine the effects of changing temperature, composition, and order of deposition upon the emerging growth patterns. In all cases, we carry out multiple simulations (typically about 5, but up to 100) using different random number seeds to govern the adsorption and diffusion events and then average the results versus time over the simulations. This diminishes the effect of any rare configuration from skewing the results and also gives a measure of statistical uncertainty.

C. Observables and KMC Results. *1. Observables Examined.* The key observables examined in the simulations, reported in the KMC results section and in the Appendix, are average island sizes versus time (where lone atoms are not counted as islands) and the surface mixing patterns. We determine an island size by "direct" bonds formed along the 4-fold fcc axis (e.g., the [011] direction) and disregard "diagonal" surface bonds (e.g., the [110] direction). In Table 2, we note that the diagonal bonding energies are 14−44% of the magnitude of the direct bonds for the EAM surface that we use (and the distinction is even clearer when islands larger than dimers are examined).

As measures of the surface patterns over time, we examine the average island size, the average pure domain island sizes (for example, the average connected pure Ni, Cu, or Pt island sizes within the overall adlayer, denoted for example as $\langle Ni \rangle$). Further measures of the surface patterns are given by the ratio of peripheral atoms of a given type

$$R_{Ni} =$$

$$\frac{\text{number of Ni atoms on the boundary of the 2D islands}}{\text{total number of atoms on the boundary of the 2D islands}}$$

$$(4)$$

and by a local order parameter that we borrow from Cowley,[44] denoted here as α and defined by

$$\alpha_{i,C,A} = 1 - A_i/M_A B_i \qquad (5)$$

where A_i is the number of A-type adatoms in the ith shell about the central adatom of type C, B_i is the number of binding sites

TABLE 3: Observable Order Parameters for Selected Extreme Cases of Two-Component, 2D Square Lattice Configurations Using Equal Numbers of the Two Components Deposited Alternately (and Using Cu/Ni Notation to Connect to Definitions in the Text)

	configuration				
parameter	random 0.2 ML	random 0.5 ML	random 1.0 ML	fully mixed	fully unmixed
$\langle size \rangle$	2.9	13.5	$(1 ML)^a$	1.0	$(0.5 ML)^a$
$\langle Ni \rangle$	2.4	3.4	13.5	1.0	$(0.5 ML)^a$
R_{Ni}	0.59	0.87	0.0	0.0	0.0
$\alpha_{1 Ni Ni}$	0.0	0.0	0.0	−1	$(+1)^b$
$\alpha_{2 Ni Cu}$	0.0	0.0	0.0	−1	$(+1)^b$

a The absolute numerical value is grid-dependent for this case, and therefore relative monolayer coverage is given. *b* The absolute numerical value is grid-dependent for this case, and the value noted is for a pure region of macroscopic size.

in the ith shell, and M_A is the total proportion of A atoms. The two shells surrounding a central atom that interest us here are indicated in Figure 1b by sites labeled "1" and "2". The order parameter essentially gives the probability of "like" or "unlike" adatoms being in the surrounding shell for each adatom being treated as the central atom. The parameter is zero for a completely random pattern of adatoms of type A and B, is positive for a more segregated than random pattern, and is negative for a less segregated than random pattern.

For comparison with values for these parameters in the KMC experiments discussed below, we give several extreme case values for these parameters in Table 3 determined by averaging three flights of 100 configurations each. The Table 3 values appear to be statistically converged to the number of figures noted. One set of extreme cases noted in Table 3 is the fully random two-component distributions using equal numbers of two adatom types deposited alternately, for a 0.2, 0.5, and the less meaningful 1.0 ML coverage of a 2D (100) lattice, as given in columns 1−3, using Cu/Ni notation for illustration purposes. The first row gives the total island size (counting both adatom types), the second row the pure-adatom island size (the same numerical value holds for $\langle Ni \rangle$ and $\langle Cu \rangle$ in these random distributions), and rows 3−5 follow from the defining order parameters of eqs 4 and 5. The other extreme cases of 1.0 ML coverage with total mixing (a perfectly alternating checkerboard pattern) and 1.0 ML coverage with no mixing (fully separated components) are also given in Table 3.

2. Composition and Bonding Pattern Comparison. In the first set of KMC simulations, we examine the effect of differing compositions of adatoms used in the deposition process on the total island size and on the pure domain island sizes (pure Cu, pure Ni, pure Pt adatom islands), always starting with the bare Ni(100) surface. For these simulations, the temperature was set to 250 K. Two different cases of mixed composition simulations are compared. One case deposits the Ni and Cu (or Pt) "sequentially", with the Ni deposited first to represent a slightly roughened Ni template upon which Cu or Pt atoms are being deposited. In the second case, the Ni and Cu (or Pt) adatoms were deposited "simultaneously" (for example, alternating −Ni−Cu−Ni−Cu− up to each type of respective coverage), giving a representation of a transition deposition from Ni to Cu/Pt with mixing that occurs as the adatoms are deposited. These two different deposition types lead to different intermediate and final growth patterns depending on the deposition time scale and the composition.

We will focus first on the case of simultaneous Ni and Cu/Pt deposition, alternating atom by atom, since it accentuates the bonding patterns that we wish to examine more closely. In
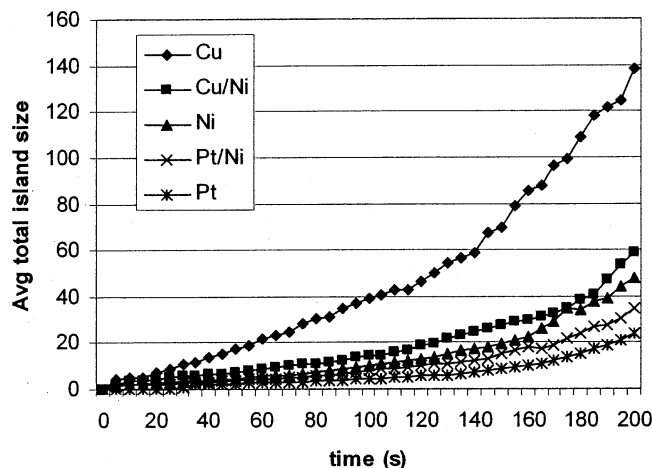
14562 *J. Phys. Chem. B, Vol. 109, No. 30, 2005*

Haug et al.

Figure 2. Total average island size vs time (in seconds) for a 500 s/ML deposition rate of either pure or alternating adatom epitaxy at 250 K. The curves from top to bottom represent pure Cu, alternating Cu/Ni, pure Ni, alternating Pt/Ni, and pure Pt.

Figure 2, we show the total average island size (counting both adatom types) versus time (in seconds) for the first 200 s using a 500 s/ML deposition rate. In this figure, from top to bottom, we show the deposition of 0.4 ML pure Cu, 0.20 ML/0.20 ML of Cu/Ni, 0.40 ML of pure Ni, 0.20 ML/0.20 ML of Pt/Ni, and 0.40 ML of pure Pt. For the results given in Figure 2, four separate iterations of the growth process are made in each case, with each iteration having on the order of 4−5 islands (for pure Cu) to 26 islands (for pure Pt) per iteration at the final deposition time of 200 s, giving a total of 16−104 islands that are averaged for the reported results. The Cu adatoms have the highest mobility on the surface, and island formation is accelerated with the presence of Cu, but in this work, it appears that the Cu is catalytically influencing the mobility of Ni adatoms in only a minor manner. For comparison, in previous work,[45,46] we reported on the catalytic ability of H adatoms on Ni island formation, via the increased mobility of Ni adatoms via the formation of H−Ni dimers. In contrast, a Ni−Cu dimer adatom behaves similar to a Ni−Ni dimer (suggested by the Table 1 energy barriers), and the slightly increasing island size for 0.20 ML/0.20 ML of Cu/Ni over 0.40 ML pure Ni can be traced predominantly to the extra mobility of the Cu adatoms alone (verified in KMC simulations by modifying the lone atom hopping barriers for Cu and Ni).

Of more interest than the total island size noted in Figure 2 is a comparison of how the nickel and copper (or platinum) atoms are distributed on the surface during and at the end of the mixed deposition/growth process. Figures 3−7 allow us to examine the segregation patterns of the growth layer. We focus on equal total compositions for the A/B systems of Cu/Ni and Pt/Ni, and in addition to the 0.40 ML coverage studies from Figure 2, we also extend the total coverage to a full monolayer, while artificially enforcing strictly 2D growth. This is nonphysical in terms of the deposition pattern since it ignores 3D growth, but it is physically meaningful in terms of the bonding energies for the 2D patterns. (Also, in test calculations including 3D effects growing a 3D fcc lattice from an initial Ni(100) face, we find that the 2D simulations appear to give equivalent growth patterns up to about the 0.7 ML total coverage, beyond which point the divergences appear to be minor. In these tests, deposition in second and third growth layers is allowed to occur onto Ni, Cu, or Pt with equal deposition rates, and the layers are offset in an ABAB pattern of the fcc lattice. Though more systematic examination is required, this near equivalence of the
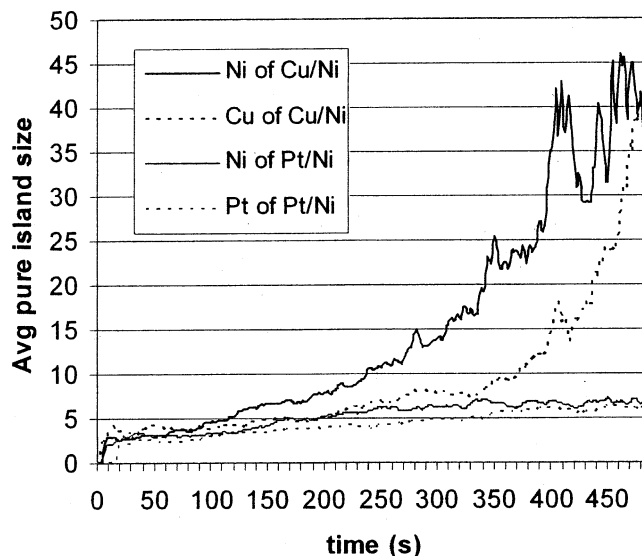

Figure 3. Average pure-adatom island size vs time (in seconds) for a 500 s/ML deposition rate of either pure or alternating adatom epitaxy at 250 K. The curves from top to bottom represent Ni during the Cu/Ni deposition, Cu during the Cu/Ni deposition, Ni during the Pt/Ni deposition, and Pt during the Pt/Ni deposition.

2D and 3D patterns appears to be due in large part because at these temperatures there is virtually no surface−adlayer exchange on the (100) surface.)

In Figure 3, the average pure-component island sizes are given for the complete monolayer growth time (at 500 s/ML t_{dep}). The two highest curves are for the Cu/Ni simultaneous deposition case; the highest curve (for the bulk of the time noted) represents the pure Ni island size, and the second highest curve is that for pure Cu. The lower two curves are for the Pt/Ni simultaneous deposition, and again the higher of the pair represents the pure Ni island size, while the lower is for pure Pt. Notable points with respect to Figure 3 can be made by comparison to the purely random configuration information given in Table 3 for selected total coverages. In a random configuration for an AB system at 0.5 ML total coverage (equal to 250 s in Figure 3), the expected average pure A or pure B island size is 3.4, while at the full 1.0 ML the expected average rises to 13.5 atoms per island. In comparison, we see that the Cu/Ni growth pattern results in Figure 3 have pure-component island sizes that rise above the random values for 250s Ni at 10.7 and Cu at 6.8 and for 500s Ni at 33.4 and Cu at 41.9. The Pt/Ni growth pattern tends to initially rise slightly above but then with increasing coverage to fall well below the random values for 250s Ni at 6.1 and Pt at 4.0 and for 500s Ni at 6.2 and Pt at 5.9. This distinction is also clearly seen in "snapshots" of the surface during the KMC growth. In Figure 4, we show a representative snapshot of the surface growth for several cases for a 40 × 40 grid. The solid dots in Figure 4 denote Ni, while the open dots denote Cu for the left column (Figures 4a−d) and Pt for the right column (Figures 4e−h). Figures 4a and 4b are results for the Cu/Ni simultaneous deposition case (a) at 250 s or 0.5 ML and (b) at 499 s or 0.99 ML, while Figures 4e and 4f are results for the Pt/Ni simultaneous deposition case (e) at 250 s or 0.5 ML and (f) at 499 s or 0.99 ML. We see that the Cu/Ni cases show substantial segregation (far more than the random deposition pattern), while the Pt/Ni cases tend to alternate in agreement with the thermodynamic tendencies based upon the Pt/Ni bond energies, but still well away from their thermodynamic limits.
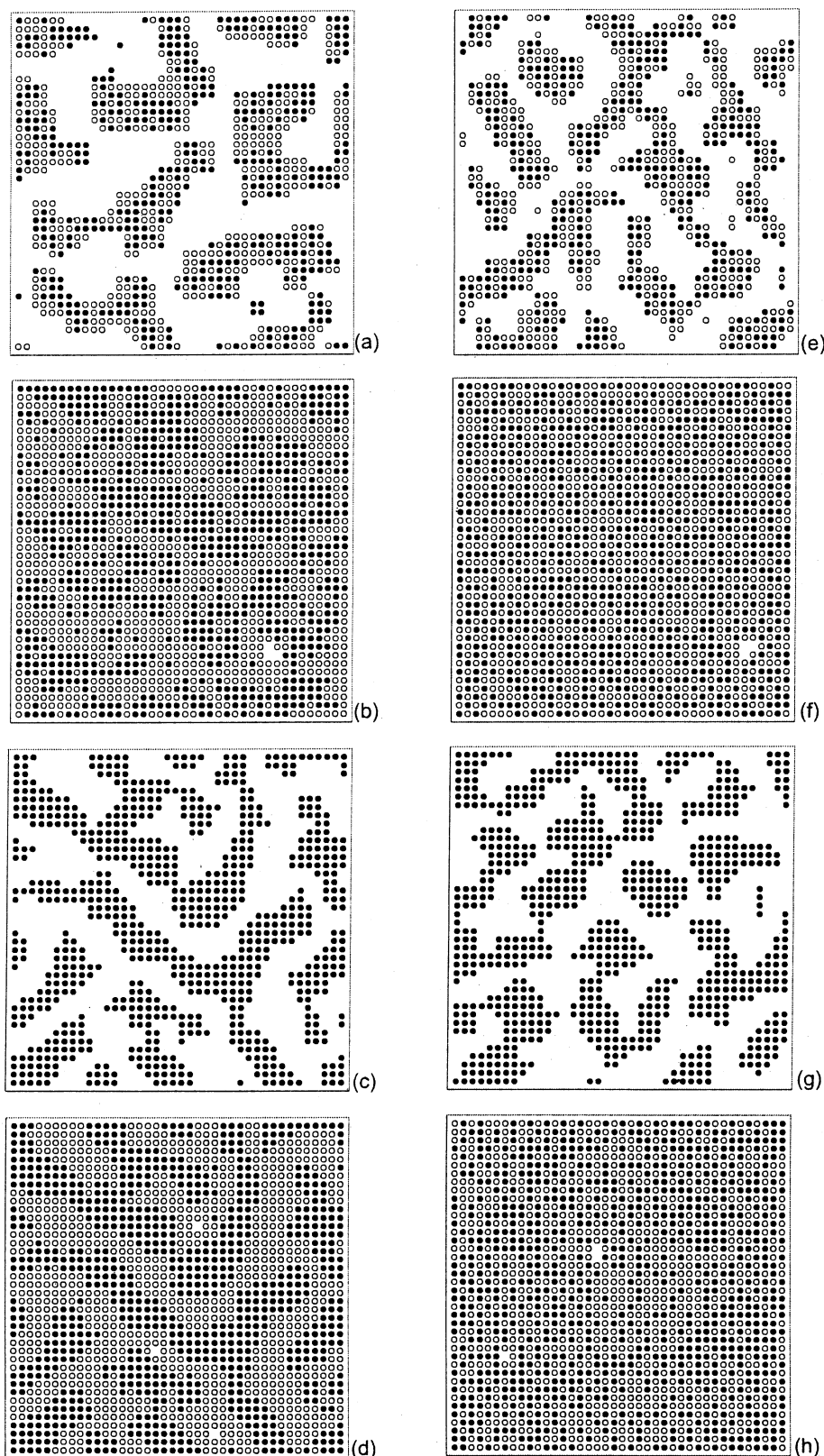
Heteroepitaxial Growth of Cu and Pt on Ni(100)

J. Phys. Chem. B, Vol. 109, No. 30, 2005 **14563**

Figure 4. Snapshots of growth patterns on a 40 × 40 grid denoting Cu/Ni in the left column and Pt/Ni in the right column. The solid dots denote Ni, while the open dots denote (a−d) Cu or (e−h) Pt. The subcomponents are for the Cu/Ni simultaneous case at (a) 0.5 and (b) 0.99 ML, for the Cu/Ni sequential case at (c) 0.5 and (d) 0.99 ML, for the Pt/Ni simultaneous case at (e) 0.5 and (f) 0.99 ML, and for the Pt/Ni sequential case at (g) 0.5 and (h) 0.99 ML.

The extent to which kinetic mixing occurs can be further seen by examining the sequential growth patterns when 0.5 ML of Ni is deposited first, followed by 0.5 ML of Cu or Pt. The remaining components of Figure 4 give snapshots of the surface for this sequential growth case. Figures 4c and 4d are results

for the Cu/Ni case (c) at 250 s or 0.5 ML and (d) at 499 s or 0.99 ML, while Figures 4g and 4h are results for the Pt/Ni case (g) at 250 s or 0.5 ML and (h) at 499 s or 0.99 ML. We see that the sequential growth case for Cu/Ni shows almost no mixing, while the Pt/Ni case tends to a final pattern nearly
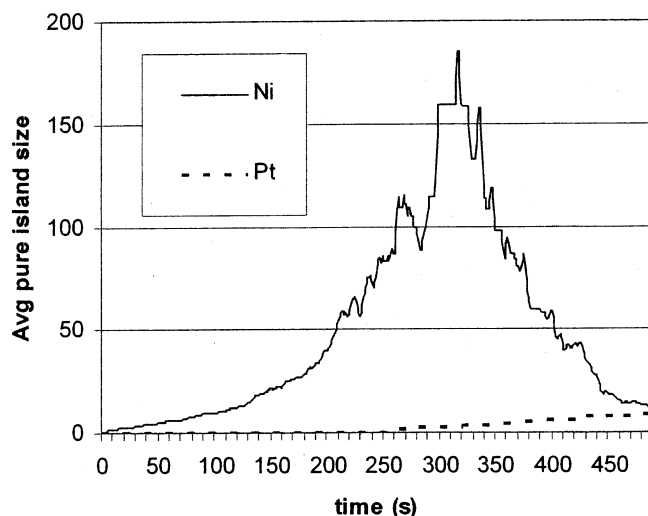
Figure 5. Average pure-adatom island size vs time (in seconds) for a 500 s/ML deposition rate of either pure-adatom epitaxy at 250 K. Pure Ni (top curve) is deposited for the first 0.5 ML, followed by pure Pt (lower curve) for the following 0.5 ML.
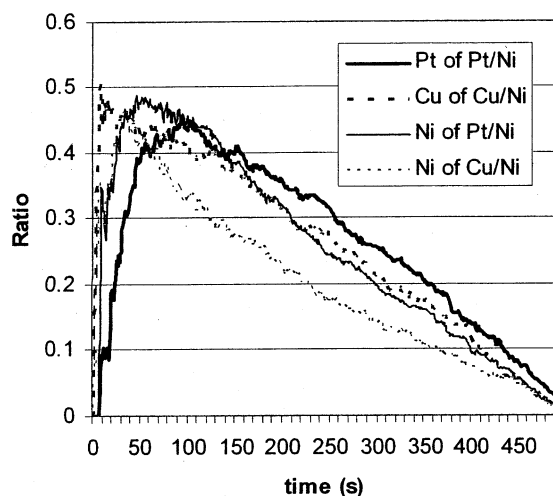

Figure 7. Average pure-adatom island size vs time (in seconds) for various deposition rates of alternating adatom epitaxy at 250 K. The curves from top to bottom represent Ni during the Cu/Ni deposition, Cu during the Cu/Ni deposition, Ni during the Pt/Ni deposition, and Pt during the Pt/Ni deposition.

Figure 6. Ratio of peripheral adatom types during simultaneous Pt/Ni and Cu/Ni growth from eq 4 versus time (in seconds). The curves from top to bottom (at 300 s) represent Pt, Cu, Ni (from Pt/Ni), and Ni (from Cu/Ni).

Figure 8. Average total island size formed during 2D growth at different temperatures. Ni and Pt atoms are deposited alternately at a 500 s/ML rate to 0.30 ML coverage. The values plotted are for temperatures from top to bottom of 325, 300, 275, and 250 K.

indistinguishable from the simultaneous growth final pattern seen by comparing Figures 4h and 4f. The final pure-component island sizes for the sequential deposition case for the Pt/Ni are a bit larger than in the simultaneous deposition case (11.2 for Ni and 8.3 for Pt in sequential growth, compared to 6.2 for Ni and 5.9 for Pt in simultaneous growth with uncertainties of about ± 0.02). The evolution in time of the Ni and Pt mixing in the sequential growth case is represented in Figure 5, where the pure Ni island size rises for about the first 300 s to over 150 atoms/island, and then falls upon continued mixing with Pt to the final value of 11.2 atoms/island. The pure Pt curve rises at 250 s with initial Pt deposition and then drifts slowly upward to the final configuration value. (The sequential Cu/Ni case is less interesting, as expected from the Figure 4 results, showing little variation with the switchover from Ni to Cu deposition, and for clarity, we do not include those results in Figure 5.)

The bonding patterns indicated in the Monte Carlo snapshots also suggest that the Cu atoms in the Cu/Ni growth scenario are preferentially found on the outer edge of the growing islands. This is confirmed in Figure 6 in which the peripheral atom ratios
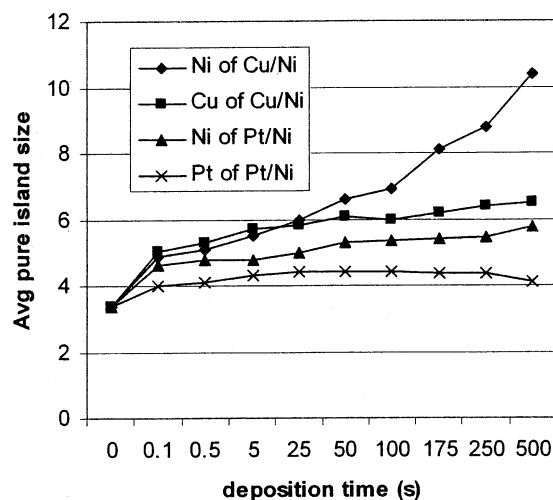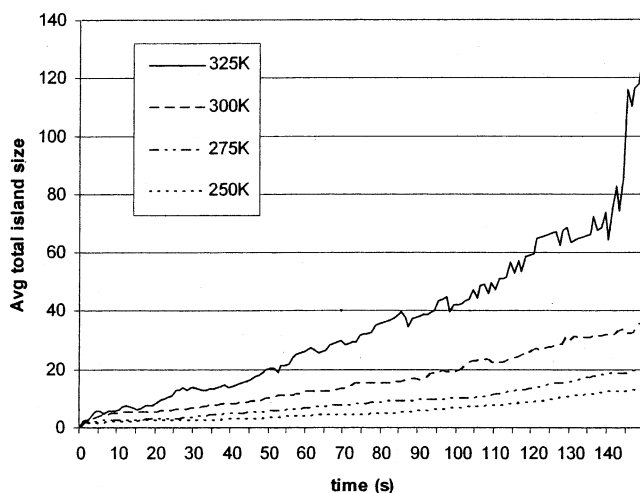
from eq 4 above are plotted over the full monolayer growth time for both the Cu/Ni and the Pt/Ni simultaneous deposition cases. The Pt and Cu both display preferred peripheral positions, with the tendency most pronounced for the Cu case. These patterns are reminiscent of those noted in previous theoretical and experimental work on bulk alloys of Cu/Ni[19−23] and Pt/Ni,[24−30] as discussed above in the Introduction. In our epitaxial work, the patterns arise for separate reasons in the Pt and Cu cases; in the Pt/Ni case, it is a kinetic effect as the relative slowness of the Pt adatom diffusion leaves them at outer island edges even though there is not a significant energy advantage (in test calculations, Pt prefers interior island sites by about 0.0028 eV per atom); in the Cu/Ni case the very mobile Cu adatoms are adjusting to a preferred energy configuration (Cu prefers exterior sites by about 0.027 eV per atom).

3. Deposition Rate Comparison. The effects of varying the deposition time (t_{dep}) over the range from 0.1 to 500 s/ML are summarized via Figure 7. In this study, $T = 250$ K, and 0.25 ML Ni/0.25 ML Cu (or Pt) are deposited using the simultaneous procedure (alternating adatom types) with the

TABLE 4: Order Parameters vs V_{Ref} for Selected Cases of Alternating Cu/Ni Deposition as Discussed in the Appendix[a]

parameter	V_{ref} (eV)								
	0.15	0.22	0.30	0.37	0.42	0.45	0.47	0.50	0.57[b]
NDRC	1417	1306	1204	1082	926	681	766	681	513
$\langle$Cu$\rangle$	5.1	5.2	5.0	5.0	5.1	4.6	4.1	4.0	3.4
$\langle$Ni$\rangle$	4.5	4.9	4.8	4.7	4.8	4.7	4.3	4.0	3.4
R_{Cu}	0.68	0.71	0.71	0.69	0.71	0.77	0.84	0.85	0.87
R_{Ni}	0.71	0.69	0.69	0.67	0.69	0.73	0.79	0.85	0.87
$\alpha_{1\ Ni\ Ni}$	−0.39	−0.45	−0.46	−0.46	−0.43	−0.41	−0.34	−0.18	0.00
$\alpha_{1\ Ni\ Cu}$	−0.46	−0.44	−0.46	−0.48	−0.46	−0.40	−0.32	−0.22	0.00

[a] The NDRC value is the total number of distinguishable rate constants out of 1489 possible. [b] This reference value for this deposition time and temperature is equivalent to a random distribution pattern.

average pure domain island sizes given at the final deposition time ($^1/_2$ of the t_{dep}). The left axis in Figure 7 (at $t_{dep}= 0$) gives the completely random pure-atom average island size for comparison purposes (determined by instantaneous deposition with no diffusion and averaged over 100 iterations). For the Cu/Ni epitaxial growth, a notable divergence between $\langle$Ni$\rangle$ and $\langle$Cu$\rangle$ is seen starting at around $t_{dep}= 50$ s and continuing across the range. Recall that, at 250K, the hopping time for a lone adatom on the Ni surface is much faster for Cu than for Ni, and Ni is much faster than the nearly immobile Pt, with lone-adatom hopping times of 5.8×10^{-3} s for Cu, 6.1×10^{-1} s for Ni, and $1.6 \times 10^{+2}$ s for Pt (although all hopping, Pt hopping in particular, is catalyzed by nearby adatoms as noted in Table 1). The shortest two of our finite deposition times are on the order of the Ni lone-atom hopping time, and the $\langle$Ni$\rangle$ and $\langle$Cu$\rangle$ curves only significantly diverge when the Ni hopping mobility dominates the deposition rate by about an order of magnitude or more. At and above this deposition time scale, the Cu/Ni thermodynamic effects noted above in the Figure 6 discussion begin to play out more fully. At shorter deposition times, the Cu/Ni patterns are becoming more kinetically trapped. While many rate processes are undoubtedly involved in this overall process, we can test the simple suggestion of a competition between Ni mobility and deposition by artificially varying the lone Ni hopping barrier. We find that artificially accelerating the Ni lone atom hopping (lowering the barrier to 0.52 eV to match the barrier of lone Cu) increases the Figure 7 trend (increasing $\langle$Ni$\rangle$ by about 30−40% for 25−250 s t_{dep} times) as the Ni islands more rapidly coalesce, while artificially slowing the Ni lone atom hopping (increasing the barrier to 0.72 eV) diminishes the trend (decreasing $\langle$Ni$\rangle$ by about 5−16% for 25−250 s t_{dep} times). In these tests, the $\langle$Cu$\rangle$ values change very little since the critical hopping time for Cu is 2 orders of magnitude faster than that for Ni. Similar results are not seen for the Pt/Ni case in Figure 7 since the interaction energy dominates their behavior as noted in the MC snapshots of Figure 4.

4. Temperature Comparison. Our temperature studies are made over a fairly small range (from 250−325 K) due to computational inefficiencies at higher T. This temperature range results in 2−3 orders of magnitude variation in adatom mobility (noted here for lone atom hopping); Cu varies from a hopping time of 5.8×10^{-3} s at 250 K to 1.7×10^{-5} s at 325 K, Ni from 6.1×10^{-1} s to 6.1×10^{-4} s, and Pt from $1.6 \times 10^{+2}$ s to 4.4×10^{-2} s. We find results that are very predictable in this range−in effect an overall acceleration of time scale. While predictable, these results do suggest that no new pathways to growth are opening over this temperature range and that therefore the pathways for growth discussed above are stable, at least over this range. As a typical example, in Figure 8, we show the total island size for the Pt/Ni simultaneous deposition case for the first 0.25 ML for a 500 s/ML deposition rate. In

Figure 8, we see that the average island size displays a gradual shift upward as a function of temperature, in agreement with expectations. (Test calculations suggest that the sudden jump for the 325 K curve at about 141 s is an artifact due to the coalescence of large islands arising from our periodic boundary conditions and the finite 40 × 40 grid size.) The Cu/Ni case displays a similar, though less pronounced pattern, since Cu is already quite mobile at 250 K, while the lone-adatom mobility of Pt is increasing from $1.6 \times 10^{+2}$ s at 250 K to 4.4×10^{-2} s at 325 K (from nearly equivalent with to well below the monolayer deposition rate constant).

III. Summary

We have calculated activation energies for a set of Cu/Ni and Pt/Ni hopping events representing 2D diffusion, island condensation, and island evaporation upon a Ni(100) substrate. The rate constants (selected values are noted in Table 1) based upon these activation energies are then used to simulate submonolayer heteroepitaxial growth via KMC simulations, and we analyze the resulting surface patterns. Our results show that Cu/Ni and Pt/Ni have different growth patterns in the temperature and deposition time regime in which we work. The key distinctions are most succinctly summarized in the growth evolution of pure-adatom domains in Figure 3 along with representative Monte Carlo snapshots shown in Figure 4, as compared to the completely random patterns documented in Table 3. The Cu/Ni systems show less than random mixing, while the Pt/Ni systems show more than random mixing, governed of course by the interaction energies (of Table 2). The Cu/Ni system has bonding energies that result in a tendency to segregate toward subdomains of pure Ni and Cu, though kinetic effects in the epitaxy trap the development of the system at arrested subdomain island sizes. The Pt/Ni system has bonding energies giving a tendency to intermix completely, while epitaxial kinetics effects modestly interfere with the complete mixing.

Appendix: Reference Rate Constant

We have tested the computational reference rate constant for the KMC simulations by both increasing and decreasing it in test case simulations. The effect of the reference rate constant is to set the clock unit time for the KMC simulation. Events occurring on a faster time scale than that given by the reference value will occur during each clock interval (but no more often), while events occurring at the reference time scale or on a slower time scale will occur in correct proportion to one another. With a finite reference time scale, we are therefore misrepresenting

some events that occur on faster time scales than the reference. As long as the misrepresented events do not significantly impact the observables, then the stochastic procedure with a fixed clock time is valid. In our study, as long as the fast time events are mainly associated with peripheral diffusion, which shifts the island edge back and forth, rather than with evaporation/ condensation events (and the two are not of course totally separable), then the island size information reported above will be unaffected by the misrepresented events. We therefore make an initial judgment regarding where to set the reference rate constant by inspection of the hopping barriers involved, but we need to test that cutoff value computationally to have a better measure of confidence in our final results. Here, we report a detailed study of the reference time scale for the Cu/Ni case only. The Cu atoms are the most mobile atoms and therefore are the most sensitive to the value of the reference energy.

In Table 4, we report a collection of the observables used in our KMC simulations at the final simulation time (0.05 s) for the following parameters: $T = 250$ K, 40×40 grid, 0.1 s deposition time with 0.25 ML Ni and 0.25 ML Cu coverage applied in an alternating ABAB pattern. The V_{ref} energy ranges from 0.15 to 0.50 eV are reported. Note that the deposition time is very short by experimental standards to allow for computational tractability at the low values of V_{ref}, but it also is long on the time scale of most of the hopping events that we are interested in distinguishing. The number of distinguished rate constants out of the total set of 1489 such rate constants is also denoted in the table, and in particular, note that at $V_{ref} = 0.15$ eV almost all of the rate constants are in fact distinguished. Note also that the values of the parameters have all broadly reached a plateau at similar values from about $V_{ref} = 0.42$ eV and below, with divergences increasing at higher values of V_{ref}. Monte Carlo standard deviations are approximately ± 2 units in the last significant figure reported for each parameter. To err a bit on the side of caution, we use $V_{ref} = 0.37$ eV for the Cu/Ni studies in the main body of this paper; however, we mainly use $V_{ref} = 0.42$ eV for the Pt/Ni studies. (The Pt adatoms are consistently less mobile than the Ni adatoms, just as the Ni adatoms are consistently less mobile than the Cu adatoms.)

References and Notes

(1) Chang, C. A. *J. Vac. Sci. Technol., A* **1990**, *8*, 3779.

(2) Gubbiotti, G.; Carlotti, G.; Minarinin, C.; Loreti, S. Gunnella, R.; De Crescenzin, M. *Surf. Sci.* **2000**, *449*, 218.

(3) Mueller, B.; Nedelmann, L.; Fischer, B.; Brune, H.; Barth, J. V.; Kern, K. *Phys. Rev. Lett.* **1998**, *80*, 2642.

(4) Fujita, T.; Tanaka, K.-I. *Surf. Sci.* **1998**, *418*, L45.

(5) Ciria, M.; Arnaudas, J. I.; del Moral, A.; O'Handley, R. C. *Phys. Rev. B* **2004**, *70*, 54431.

(6) Lee, J. S.; Lee K. B.; Park Y. J.; Kim, T. G.; Song, J. H.; Chae, K. H.; Lee, J.; Whang, C. N.; Jeong, K.; Kim, D. H.; Shin, S. C. *Phys. Rev. B* **2004**, *69*, 172405.

(7) Semancik, S.; Cavicchi, R. E.; Kreider, K. G.; Suehle, J. S.; Choparala, P. *Sens. Actuators, B* **1996**, *34*, 209.

(8) Richardson, J. T. *Principles of Catalyst Development*; Plenum: New York, 1989.

(9) Campbell, C. T. *Annu. Rev Phys. Chem.* **1990**, *41*, 775.

(10) Chen M. S.; Goodman, D. W. *Science* **2004**, *306*, 252.

(11) Stamenkovic, V.; Schmidt, T. J.; Ross, P. N.; Markovic, N. M. *J. Phys. Chem. B* **2002**, *106* 11970.

(12) Winans, R. E.; Vajda, S.; Lee, B.; Riley, S. J.; Seifert, S.; Tikhonov, G. Y. Tomczyk, N. A. *J. Phys. Chem. B* **2004**, *108*, 18105.

(13) Cheng, W. H.; Wu, K. C.; Lo, M. Y.; Lee, C. H. *Catal. Today* **2004**, *97*, 145.

(14) Castellani, N. J.; Mehadji, C.; Legare, P. *Surf. Rev. Lett.* **1997**, *4*, 45.

(15) Hwu, H. H.; Eng, J., Jr.; Chen, J. G. *J. Am. Chem. Soc.* **2002**, *124*, 702.

(16) Larsson, M. I.; Sabiryanov, R. F.; Cho, K. Clemens, B. M. *Surf. Sci.* **2003**, *536*, L389.

(17) Jensen, P. *Rev. Mod. Phys.* **1999**, *71*, 1695.

(18) Foiles, S. M.; Baskes, M. I.; Daw, M. S. *Phys. Rev. B* **1996**, *33*, 7983.

(19) Foiles, S. M. *Phys. Rev. B* **1985**, *32*, 7685.

(20) Webber, P. R.; Rojas, C. E.; Dobson, P. J.; Chadwick, D. *Surf. Sci.* **1981**, *105*, 20.

(21) Wandelt, K.; Brundle, C. R. *Phys. Rev. Lett.* **1981**, *46*, 1529.

(22) Ng, Y. S.; Tsong, T. T.; McLane, S. B., Jr. *Phys. Rev. Lett.* **1979**, *42*, 588.

(23) Brongersma, H. H.; Sparnay, M. J.; Buck, T. M. *Surf. Sci.* **1978**, *71*, 657.

(24) Lundberg, M. *Phys. Rev. B* **1987**, *36*, 4692.

(25) Pourovskii, L. V.; Ruban, A. V.; Abrikosov, I. A.; Vekilov, Y. Kh.; Johansson, B. *Phys. Rev. B* **2001**, *64*, 35421.

(26) Gauthier, Y.; Joly, Y.; Baudoing, R.; Rundgren, J. *Phys. Rev. B* **1985**, *31*, 6216.

(27) Gauthier, Y.; Baudoing, R.; Laundgren, M.; Rundgren, J. *Phys. Rev. B* **1987**, *35*, 7867.

(28) Dufayard, R.; Baudoing, R.; Gauthier, Y. J. *Surf. Sci.* **1990**, *233*, 223.

(29) Deckers, S.; Habraken, F. H. P. M.; van der Weg, W. F.; Denier van der Gonm, A. W.; Pluid, B.; vand der Veen, J. F.; Baudoing, R. *Phys. Rev. B* **1990**, *42*, 3253.

(30) Gauthier, Y.; Baudoing-Savois, R.; Rundgren, J.; Hammar, M.; Gothelid, M. *Surf. Sci.* **1995**, *327*, 100.

(31) Wang, G.; Van Hove, M. A.; Ross, P. N.; Baskes, M. I. *J. Chem. Phys.* **2005**, *122*, 0 24706.

(32) Haug, K.; Do, N. K. N. *Phys. Rev. B* **1999**, *60*, 11095.

(33) Plimpton, S. J.; Hendrickson, B. A. In *Materials Theory and Modeling*; Broughton, J., Bristowe, P., Newsam, J., Eds.; Materials Research Society Symposia Proceedings 291, Materials Research Society: Pittsburgh, PA, 1993. The particular code used, ParaDyn, was obtained from S. J. Plimpton at Sandia National Laboratory through private communication. We use the cuu3, niu3, and ptu3 EAM potentials that are available with that program. Details of ParaDyn are available in the reference noted.

(34) Over 1200 citations to ref 18 can be found (from the Web of Science) that we will not try to summarize, but that include applications involving molecular dynamics, Monte Carlo simulations, vibrational dynamics, and structural and energetic properties.

(35) Tung, R. T.; Graham, W. R. *Surf. Sci.* **1980**, *97*, 73.

(36) Fichthorn, K. A.; Weinberg, W. H. *J. Chem. Phys.* **1991**, *95*, 1090.

(37) Haug, K.; Zhang, Z.; John, D.; Walters, C. F.; Zehner, D. M.; Plummer, W. E. *Phys. Rev. B* **1997**, *55*, R10233−R10236.

(38) Liu, Y.-T.; Metiu, H. *Surf. Sci.* **1991**, *245*, 150.

(39) Uebing, C. In *Surface Diffusion: Atomistic and Collective Processes*; Tringides, M. C., Ed.; Plenum: New York, 1997.

(40) Owens, T. O.; Krishnan, S.; Alameda, J.; Braatz, R. D.; Alkire, R. C. *AIChE J.* **2004**, *50*, 226.

(41) Owens, T. O.; Web., E. G.; Ma, D. L.; Alameda, J.; Gannon, D.; Braatz, R. D.; Alkire, R. C. *IBM J. Res. Dev.* **2005**, *49*, 49.

(42) Uebing, C.; Gomer, R. *J. Chem. Phys.* **1991**, *95*, 7626.

(43) Bortz, A. B.; Kalos, M. H.; Lebowitz, J. L. *J. Comput. Phys.* **1975**, *17*, 10.

(44) Cowley, J. M. *Phys. Rev.* **1950**, *77*, 669.

(45) Haug, K.; Jenkins, T. J. *Phys. Chem. B* **2000**, *104*, 10017.

(46) Haug, K.; Jamhoury, J. *Phys. Chem. B* **2002**, *106*, 11253.